Earth Planet. Sci. Lett. **81**, 175 (1987).
3. W.-X. Li *et al.*, *Nature* **339**, 534 (1989).
4. E. Bard, B. Hamelin, R. G. Fairbanks, A. Zindler, *ibid.* **345**, 405 (1990).
5. Stable isotopic analyses were performed at the Univ. of Michigan Stable Isotope Laboratory. Values of $\delta^{13}C$ are reported relative to PDB and $\delta^{18}O$ values relative to SMOW. Reported precision is better than ±0.05 per mil.
6. R. S. Harmon, H. P. Schwarcz, D. C. Ford, D. L. Koch, *Geology* **7**, 430 (1979).
7. To preserve the ornamentation of Cold Water Cave, we restored the stalagmite to its original position after coring.
8. Preliminary U-Th ages were determined by alpha spectrometry at the University of Iowa. Powdered samples ranging from 0.6 to 2.1 grams were dissolved in 4 N HNO_3 by slow titration at room temperature, centrifuged, and separated from submilligram silicate residues. Samples were spiked with ^{228}Th-^{232}U, and U and Th were purified by anion exchange chromatography. Counting times lasted 10 to 14 days, and counts were corrected for tailing and background contamination. Mass spectrometric analyses were performed at the Los Alamos National Laboratory. Samples of 0.2 to 0.9 grams were prepared by a method similar to alpha-dated samples with the use of 1.5 N HNO_3 for dissolution and spiked with ^{229}Th-^{233}U-^{236}U. The residue from the largest sample (MS-1) was analyzed for purposes of correction [T. L. Ku and Z. C. Liang, *Nuclear Instr. Methods Phys. Res.* **223**, 563 (1984)]. The ratio of ^{230}Th to ^{232}Th of the residue was 2.5×10^{-6}, a value typical for silicate rocks (for example, clay minerals). A National Bureau of Standards–designed, 30.5-cm radius, 90° deflection, single magnetic sector thermal ionization instrument equipped with ion counting detection systems was used to determine U concentrations and isotopic compositions. Measurements of Th were obtained on a similar instrument with two magnetic sectors in an "S" configuration. Details of the mass spectrometry procedure are described in S. J. Goldstein, M. T. Murrell, D. R. Janecky, *Earth Planet. Sci. Lett.* **96**, 134 (1989).
9. C. H. Hendy, *Geochim. Cosmochim. Acta* **35**, 801 (1971).
10. P. Fritz, R. J. Drimmie, S. K. Frape, K. O'Shea, in *Proceedings of the International Symposium on Isotope Techniques in Water Resources Development* (International Atomic Energy Agency, Vienna, Austria, 1987), pp. 539–550.
11. C. J. Yonge, D. C. Ford, J. Gray, H. P. Schwarcz, *Chem. Geol. Isot. Geosci. Sect.* **58**, 97 (1985).
12. R. S. Harmon, *Water Resour. Res.* **15**, 503 (1979).
13. L. A. González and K. C. Lohmann, in *Paleokarst*, N. P. James and P. W. Choquette, Eds. (Springer, New York, 1988), pp. 81–101.
14. K. C Lohmann, in *ibid.*, pp. 58–80.
15. J. R. Gat, in *Proceedings of the International Symposium on Isotope Techniques in Water Resources Development* (International Atomic Energy Agency, Vienna, Austria, 1987), pp. 551–563.
16. W. Dansgaard, *Tellus* **16**, 438 (1964).
17. Y. Yurtsever and J. R. Gat, in *Deuterium and Oxygen 18 in the Water Cycle*, J. R. Ford and R. Gonfiantini, Eds. (International Atomic Energy Agency, Vienna, Austria, 1980), pp. 103–142.
18. G. W. Moore and G. N. Sullivan, *Speleology* (Zephyrus, Teaneck, NJ, ed. 2, 1978).
19. J. R. O'Neil, R. N. Clayton, T. J. Mayeda, *Chem. Phys.* **30**, 5547 (1969).
20. B. Turi, in *Handbook of Environmental Isotope Geochemistry. The Terrestrial Environment, Part B*, P. Fritz and J. C. Fontes, Eds. (Elsevier, New York, 1986), pp. 207–238.
21. T. E. Cerling, *Earth Planet. Sci. Lett.* **71**, 229 (1984).
22. P. Deines, in *Handbook of Environmental Isotope Geochemistry. The Terrestrial Environment, Part A*, P. Fritz and J. Ch. Fontes, Eds. (Elsevier, New York, 1980), pp. 331–406.
23. D. J. Ode and L. J. Tieszen, *Ecology* **61**, 1304 (1980).
24. J. A. Teeri and L. G. Stowe, *Oecologia* **23**, 1 (1976).
25. J. D. Hudson, *Geol. Soc. London* **33**, 637 (1977).
26. K. L. Van Zant, *Quat. Res.* **12**, 358 (1979).
27. R. G. Baker, C. A. Chumbley, P. M. Witinok, H. K. Kim, *J. Iowa Acad. Sci.* **97**, 167 (1990).
28. C. A. Chumbley, R. G. Baker, E. A. Bettis III, *Science* **249**, 272 (1990).
29. Ages of pollen and plant macrofossil sites are routinely reported in radiocarbon years before present. We have converted radiocarbon years to years before present using data or figures (or both) in G. W. Pearson, J. R. Pilcher, M. G. L. Baillie, D. M. Corbett, and F. Qua [*Radiocarbon* **28**, 911 (1986)]; and in M. Stuiver, B. Kromer, B. Becker, and C. W. Ferguson [*ibid.*, p. 969].
30. C. A. Chumbley, thesis, University of Iowa (1989).
31. For the 25-year mean annual surface temperature over Cold Water Cave (7.3°C), Dansgaard's relation $\delta^{18}O_p = 0.695(t) - 13.6$ (*16*) yields a $\delta^{18}O_p$ value of −8.53 per mil, which is nearly identical to the $\delta^{18}O$ value for local shallow ground waters of −8.50 per mil (S. J. Kalhkof, personal communication).
32. I. Friedman and J. R. O'Neil, in *U.S. Geol. Surv. Prof. Paper 440-KK* (1977).
33. J. E. Kutzbach and T. Webb III, in *Quaternary Landscapes*, L. C. K. Shane and E. J. Cushing, Eds. (Univ. of Minnesota Press, Minneapolis, 1991), pp. 175–218.
34. R. A. Bryson, *Geogr. Bull.* **8**, 228 (1966).
35. W. L. Prell, J. V. Gardner, A. W. Be, J. D. Hays, *Geol. Soc. Am. Mem.* **145**, 247 (1976).
36. W. H. Schlesinger, *Annu. Rev. Ecol. Syst.* **8**, 51 (1977).
37. C. T. Rightmire and B. B. Hanshaw, *Water Resour. Res.* **9**, 958 (1973).
38. P. J. Bartlein, T. Webb III, E. Fleri, *Quat. Res.* **22**, 361 (1984).
39. W. A. Watts and R. C. Bright, *Geol. Soc. Am. Bull.* **79**, 855 (1968).
40. R. G. Baker, L. J. Maher, C. A. Chumbley, K. A. Van Zant, *Quat. Res.* **37**, 379 (1992).
41. J. H. McAndrews, *Mem. Torrey Bot. Club* **22**, 1 (1966).
42. E. A. Bettis III, personal communication.
43. We thank the Cold Water Cave owners K. and W. Flatland for granting access to the cave and M. Bounk, S. Barnett, P. Knoerr, and S. Moon for assistance. Supported by grants from the Littlefield fund and the Sedimentary Geochemistry Laboratory (to J.D.) and the Center for Regional and Environmental Research, University of Iowa (to L.G. and M.K.R.). Support for this research at Los Alamos National Laboratory was provided by a grant from the Geosciences Research Program (Department of Energy, Office of Basic Energy Science) (to M.T.M. and D.A.P.). Iowa Quaternary Studies Group Contribution 55.

13 July 1992; accepted 1 October 1992

Direct Detection of C_4H_2 Photochemical Products: Possible Routes to Complex Hydrocarbons in Planetary Atmospheres

Ralph E. Bandy, Chitra Lakshminarayan, Rex K. Frost, Timothy S. Zwier*

The photochemistry of diacetylene (C_4H_2), the largest hydrocarbon to be unambiguously identified in planetary atmospheres, is of considerable importance to understanding the mechanisms by which complex molecules are formed in the solar system. In this work, the primary products of C_4H_2's ultraviolet photochemistry were determined in a two-laser pump-probe scheme in which the products of C_4H_2 photoexcitation are detected by vacuum ultraviolet photoionization in a time-of-flight mass spectrometer. Three larger hydrocarbon primary products were observed with good yield in the $C_4H_2^* + C_4H_2$ reaction: C_6H_2, C_8H_2, and C_8H_3. Neither C_6H_2 nor C_8H_3 is anticipated by current photochemical models of the atmospheres of Titan, Uranus, Neptune, Pluto, and Triton. The free hydrogen atoms that are released during the formation of the C_8H_3 and C_8H_2 products also may partially offset the role of C_4H_2 in catalyzing the recombination of free hydrogen atoms in the planetary atmospheres.

Diacetylene (C_4H_2) plays a role in the stratospheres of several of the solar system's planets and moons analogous to that played by O_3 in Earth's atmosphere. The absorptions of C_4H_2, like O_3, serve as an effective ultraviolet radiation shield for the lower atmosphere and planetary surface. Yet, like O_3, C_4H_2 is photochemically reactive (*1*) and is postulated as the primary source of yet larger hydrocarbons in these atmospheres (*2*–*6*). Despite the importance of C_4H_2, the products of C_4H_2 photochemistry in the ultraviolet are not known. As a result, the current photochemical models of Titan (*2*), Uranus (*3*), Neptune (*4*), Pluto (*5*), and Triton (*6*) postulate that C_8H_2 is the sole primary product of C_4H_2's self-reaction. This report presents results of a photochemical study of C_4H_2 in which the primary photochemical products of the $C_4H_2^*$ (excited state) + C_4H_2 reaction are unambiguously identified. Three primary products are observed with good yield: C_6H_2 (+ C_2H_2), C_8H_2 (+ H_2, 2H), and C_8H_3 (+ H). Secondary products formed by subsequent reaction of the primary products with C_4H_2 are dominated by $C_{10}H_3$ and $C_{12}H_3$.

The methods used to synthesize and handle C_4H_2 have been described (*7*). The

Department of Chemistry, Purdue University, West Lafayette, IN 47907.

*To whom correspondence should be addressed.

photochemistry is carried out just outside the ion source region of a time-of-flight mass spectrometer (8). The doubled output of an excimer-pumped dye laser (Lambda Physik LPX/FL3002) tunable from 245 to 220 nm is used to excite C_4H_2 to various vibronic levels in the $^1\Delta_u$ excited state (7). This photoexcitation laser is counterpropogated down a 5-mm length of quartz tube (2 mm in diameter) through which the mixture of 1 to 10% C_4H_2 in He is introduced by means of a pulsed valve. The C_4H_2* reacts with C_4H_2 during its 10-μs traversal of the reaction tube. The products of the reaction are subsequently photoionized 7 cm from the end of the reaction tube with 118-nm light (10.5 eV) produced by tripling the 355-nm output of a Nd:yttrium-aluminum-garnet laser in Xe gas (9). The photoions are mass-analyzed in a linear time-of-flight mass spectrometer and detected with a microchannel plate ion detector. Because the $C_4H_2^+$ reactant ion signal is nearly 1000 times the size of the product signals, a 1.0-μs-long, +800-V pulse is applied to a steering plate in the time-of-flight tube to deflect away the $C_4H_2^+$ ions before their arrival at the ion detector.

Time-of-flight mass spectra were taken with and without the photoexcitation laser present under conditions optimized for the detection of photochemical products (Fig. 1, A and B). The difference mass spectrum (Fig. 1C) highlights the products of C_4H_2 photochemistry. The mass 86 and 88 peaks present in Fig. 1, A and B, are due to minor impurities of 2-chloro-2-butene-3-yne present in the C_4H_2 sample from its synthesis. The total integrated intensity of all C_4H_2 photochemical products is about 0.2% of the $C_4H_2^+$ reactant ion signal (not shown).

Action spectra (Fig. 2) confirm that the products observed are the result of gas phase photochemical reactions of C_4H_2. In performing a resonant two-photon ionization scan (Fig. 2, curve a), we used the photoexcitation laser both to excite the neutral C_4H_2 molecules and subsequently to ionize them directly in the ion source of the time-of-flight mass spectrometer. The dominant absorption feature is the $2^1_0 6^1_0$ vibronic transition of the $^1\Delta_u \leftarrow {}^1\Sigma_g^+$ band at 231.3 nm, observed earlier by Bandy *et al.* (7) and others (10). Action spectra taken by tuning the photoexcitation laser while monitoring $C_6H_2^+$, $C_8H_2^+$, $C_8H_3^+$, and $C_{10}H_3^+$ are shown in Fig. 2, curves b through e, respectively. Both the faithful reproduction of C_4H_2's absorption spectrum by the product masses and the linear dependence of the primary product signals on the photoexcitation laser power demonstrate that the primary products (Fig. 2, curves b through d) result from the absorption of a single photon by gas-phase C_4H_2.

Glicker and Okabe (1) have determined a photochemical quantum yield for loss of C_4H_2 at 2.0 ± 0.5 over the wavelength range of interest here. The present results demonstrate that three primary photochemical reaction channels are responsible for the loss of C_4H_2 after excitation in the range 245 to 220 nm:

$$C_4H_2^* + C_4H_2 \rightarrow C_6H_2 + C_2H_2 \quad (1)$$

$$\rightarrow C_8H_2 + H_2 \text{ (or } 2H) \quad (2)$$

$$\rightarrow C_8H_3 + H \quad (3)$$

The distribution of product ion intensities is only weakly dependent on the excitation wavelength over the range 245 to 220 nm, even though this range extends below the lowest dissociation limit for the molecule. This result confirms the deduction of Glicker and Okabe (1) that, at the reaction tube pressures of our studies (~10 torr total pressure), bound metastable states of C_4H_2 are responsible for the photochemistry rather than free-radical reactions arising from direct photolysis.

The relative yields of C_8H_2 and C_8H_3 depend sensitively on the C_4H_2 concentration, the time spent in the reaction tube, and the nature and amount of buffer gas. One route for the formation of C_8H_2 is likely to be loss of H_2 from the C_8H_4* reaction complex. However, as Fig. 3 shows, if H atom loss from C_8H_4* forms vibrationally excited C_8H_3† with

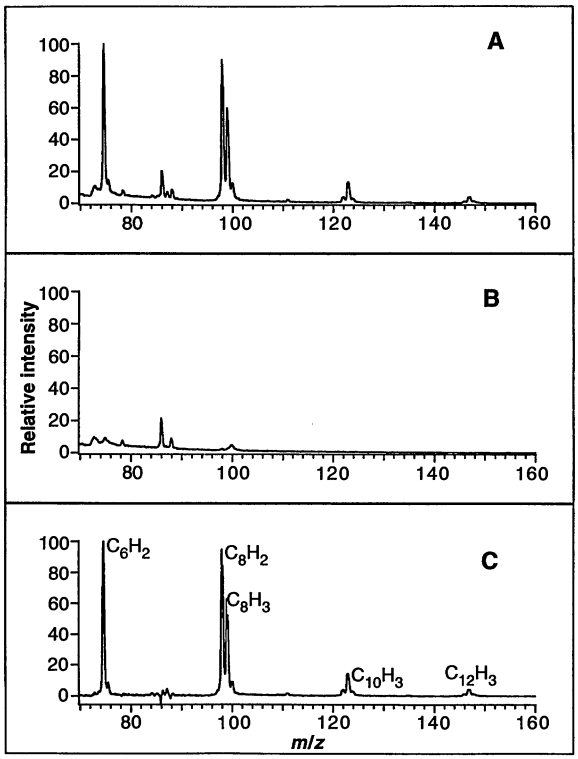

Fig. 1. Time-of-flight mass spectra after vacuum-ultraviolet photoionization: (**A**) with the photoexcitation laser on, (**B**) with the photoexcitation laser off, and (**C**) the difference between (A) and (B), highlighting the products of C_4H_2 photochemistry; *m/z*, mass-to-charge ratio. The mass 78, 86, and 88 ions present in both (A) and (B) are impurity ions in the C_4H_2 sample. The peak corresponding to the $C_4H_2^+$ ion arising from C_4H_2 reactants (not shown) is about 1000 times the size of the product peaks shown.

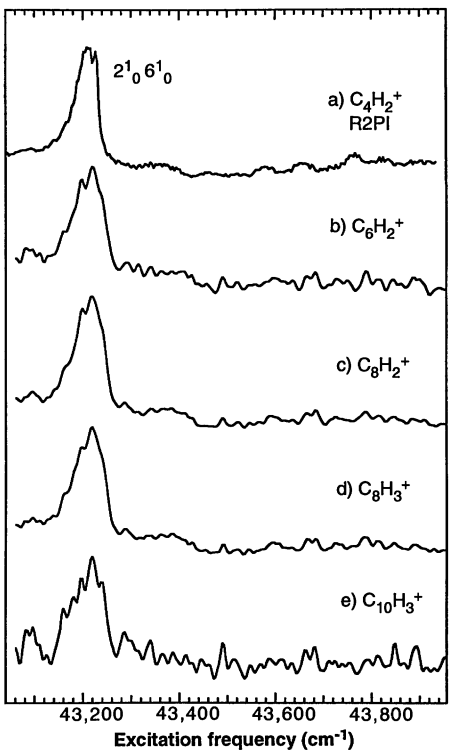

Fig. 2. Curve a: Resonant two-photon ionization scan (R2PI) in the $2^1_0 6^1_0$ region of the $^1\Delta_u \leftarrow {}^1\Sigma_g^+$ transition of C_4H_2 monitoring the $C_4H_2^+$ mass. Curves b through e: Action spectra of the photochemical products $C_6H_2^+$, $C_8H_2^+$, $C_8H_3^+$, and $C_{10}H_3^+$ in the $2^1_0 6^1_0$ region recorded with both photoexcitation and photoionization lasers present. The close correspondence of the scans shows that the observed products arise from photoexcitation of gas phase C_4H_2.

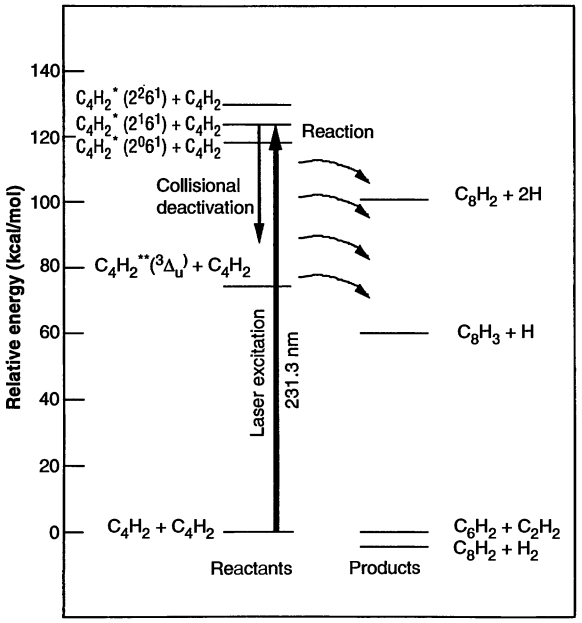

Fig. 3. Schematic energy level diagram of C_4H_2's ultraviolet photochemistry. The $^3\Delta_u$ state is a metastable state of C_4H_2. The extent of collisional deactivation of the reactant $C_4H_2^*$ species can affect the distribution of products formed. The reaction enthalpies are estimates based on extrapolation of the heats of formation of C_2H_2, C_2H_3, and C_4H_2 (*11*) to the larger C_nH_2 and C_nH_3 species.

enough internal energy, it can undergo loss of a second H atom to form C_8H_2:

$$C_4H_2^* + C_4H_2 \rightarrow C_8H_4^* \quad (4a)$$

$$C_8H_4^* \rightarrow C_8H_3\dagger + H \quad (4b)$$

$$C_8H_3\dagger \rightarrow C_8H_2 + H \quad (4c)$$

Furthermore, the highly reactive C_8H_3 radical can react with C_4H_2 by H atom exchange driven by the reaction exothermicity:

$$C_8H_3\dagger + C_4H_2 \rightarrow C_4H_3 + C_8H_2 \quad (5)$$

As a result, gas mixtures with high N_2 and low C_4H_2 concentrations (that is, conditions that minimize reactions 4c and 5, respectively) increase the C_8H_3 product signal to roughly twice that of C_8H_2. On the other hand, conditions that provide short reaction times and minimal collisional deactivation almost completely eliminate the C_8H_3 product signal from the time-of-flight mass spectrum. Despite the sensitivity of the C_8H_3/C_8H_2 product ratio, the relative yield of C_6 to C_8 products is much less sensitive to changing conditions than the C_8H_3/C_8H_2 ratio.

For a given set of reaction conditions, the ratio of two product ion intensities, $I_{prod}(1)/I_{prod}(2)$, is given by

$$\frac{I_{prod}(1)}{I_{prod}(2)} = \frac{\phi_{prod}(1)\sigma_{PI}(1)\, f_{det}(1)}{\phi_{prod}(2)\, \sigma_{PI}(2)\, f_{det}(2)} \quad (6)$$

where $\phi_{prod}(m)$ is the quantum yield for formation of product m under these conditions, $\sigma_{PI}(m)$ is the 118-nm photoionization cross section of product m, and f_{det} is the fraction of product m entering the photoionization laser interaction volume. Because the reaction occurs primarily within the confines of the reaction tube, differences in the fraction of products collected should not be large. Quantitative measurements of the 118-nm photoionization cross sections are not currently available for the product molecules. However, the photoionization cross sections for the C_6H_2 and C_8H_2 products should be similar by virtue of their similar chemical structure. In addition, the transfer in intensity between $C_8H_2^+$ and $C_8H_3^+$ with changing N_2 pressure (that is, with decreasing reactant internal energy) suggests that the 118-nm photoionization cross sections for C_8H_2 and C_8H_3 are also roughly similar. As a reasonable first estimate, then, the relative photochemical quantum yields for a given reaction mixture follow directly from the relative intensities of the product ions, normalized to a total quantum yield of two.

From the standpoint of reaction dynamics, perhaps the most intriguing product channel observed is the $C_6H_2 + C_2H_2$ channel. The C_2H_2 product is not directly observed in this experiment because its ionization potential (11.4 eV) is greater than the vacuum-ultraviolet photon energy (10.5 eV). The extensive rearrangement that accompanies formation of $C_6H_2 + C_2H_2$ in a $C_4H_2^* + C_4H_2$ collision will require further study if we are to understand the mechanism for its formation.

In addition to the primary products, also present are small amounts of secondary products, formed by the subsequent reaction of the primary products with C_4H_2. The $C_{10}H_3$ and $C_{12}H_3$ products dominate the secondary products observed. Thermochemical considerations point to C_8H_3 as the primary product responsible for $C_{10}H_3$ and $C_{12}H_3$ formation because its reactions with C_4H_2

$$C_8H_3 + C_4H_2 \rightarrow C_{10}H_3 + C_2H_2 \quad (7a)$$

$$C_8H_3 + C_4H_2 \rightarrow C_{12}H_3 + H_2 \quad (7b)$$

are near thermoneutral (*11*) and thus could be driven by the primary reaction exothermicity. These products may represent the initial steps toward the polymer formation that is the final end product of ultraviolet irradiation of gas phase C_4H_2.

The present results may have significant consequences for current photochemical models of hydrocarbon-rich planetary atmospheres. Glicker and Okabe's work on C_4H_2 (*1*) has established that the metastable state of C_4H_2 is not quenched even by thousands of collisions with H_2 or N_2, two major constituents of Titan's atmosphere. As a result, despite the small concentration of C_4H_2 in many of the planetary atmospheres, $C_4H_2^* + C_4H_2$ photochemistry may represent an important route to the formation of larger hydrocarbons on Titan and the outer planets. The unanticipated C_8H_3 product may be especially important because it provides an entry point to free-radical processes even below the threshold for direct photolysis of C_4H_2. As a free radical, C_8H_3 may react readily with a wide range of hydrocarbons. Our results provide some evidence in support of this contention in the dominance of $C_{10}H_3$ and $C_{12}H_3$ over other secondary products.

Finally, the present results also impact planetary modeling in the free H atoms that are produced in reactions 3 and 4. The current models of CH_4 photochemistry postulate a scheme (*2–6*) for recombining H atoms from the stratosphere which uses C_4H_2 as catalyst:

$$C_4H_2 + H + M \rightarrow C_4H_3 + M \quad (8a)$$

$$C_4H_3 + H \rightarrow C_4H_2 + H_2 \quad (8b)$$

However, the present results indicate that C_4H_2 photochemistry produces free H atoms in both the $C_8H_3 + H$ and $C_8H_2 + 2H$ channels. Thus, C_4H_2 photochemistry also plays a role as a source of free H atoms, counteracting the molecule's role as a catalyst for H atom recombination.

REFERENCES AND NOTES

1. S. Glicker and H. Okabe, *J. Phys. Chem.* **91**, 437 (1987).
2. Y. L. Yung, M. Allen, J. P. Pinto, *Astrophys. J. Suppl. Ser.* **55**, 465 (1984); Y. L. Yung, *Icarus* **72**, 468 (1987).
3. S. K. Atreya, B. R. Sandel, P. N. Romani, in *Uranus*, J. T. Bergstrahl, Ed. (Univ. of Arizona Press, Tucson, 1990), pp. 110–146; M. E. Summers and D. F. Strobel, *Astrophys. J.* **346**, 495 (1989); J. B. Pollack *et al.*, *J. Geophys. Res.* **92**, 15037 (1987).
4. P. N. Romani and S. K. Atreya, *Icarus* **74**, 424 (1988); *Geophys. Res. Lett.* **16**, 941 (1989).
5. J. A. Stansberry, J. I. Lunine, M. G. Tomasko, *Geophys. Res. Lett.* **16**, 1221 (1989).
6. W. R. Thompson, S. K. Singh, B. N. Khare, C. Sagan, *ibid.*, p. 1981.
7. R. E. Bandy, C. Lakshminarayan, T. S. Zwier, *J. Phys. Chem.* **96**, 5337 (1992).

8. A. J. Gotch and T. S. Zwier, *J. Chem. Phys.* **96**, 3388 (1992).
9. See, for example, R. Mahon, T. J. McIlrath, V. P. Myerscough, D. W. Koopman, *IEEE J. Quantum Electron.* **QE-15**, 444 (1979).
10. K. W. Chang and W. R. M. Graham, *J. Mol. Spectrosc.* **94**, 69 (1982); H.-J. Haink and M. Jungen, *Chem. Phys. Lett.* **61**, 319 (1979).
11. S. G. Lias, J. E. Bartmess, J. L. Holmes, R. D. Levin, W. G. Mallard, *J. Phys. Chem. Ref. Data* **17**, 82 (1988).
12. This work was supported by the National Aeronautics and Space Administration Planetary Atmospheres Program.

28 July 1992; accepted 2 October 1992

Production and Initial Characterization of Bionites: Materials Formed on a Bacterial Backbone

Neil H. Mendelson

The addition of soluble metal salts of calcium, iron, or copper to cultures of *Bacillus subtilis* grown in web form nucleated precipitation at the surface of the bacterial cell walls. The mineralized cell filaments can be drawn into a fiber that when dried consists of a bacterial thread backbone carrying an inorganic solid. The ratios of organic to inorganic components (by weight) in the stiff brittle materials, called bionites, were: 1.08 for fe(2)bactonite, 1.8 for calbactonite, 2.3 for fe(3)bactonite, and 5 for cu(2)bactonite. X-ray photoelectron spectra suggest that the fe(3)bactonite contains Fe_2O_3, that calbactonite contains calcium carbonate, and that cu(2)bactonite contains CuCl (Cu I). Acid-base reactions of the bionites are compatible with these identifications. Burning out the organic phase of the febactonites yields a black magnetic material, presumably magnetite. The burnt cubactonite appears to yield elemental Cu(s). Calbactonite upon hydration was able to retain a genetically engineered enzymatic activity.

Recent advances in biotechnology have provided new tools for the manipulation of biological materials and the production of chemical products (*1*). Similar approaches have yet to be applied to materials synthesis. This report describes a system in which it may be possible to do so. The basic idea is to use bacterial cell walls in situ as a matrix for mineralization and to draw the products (*2*) into fiberlike materials. Three such products, called bionites, are described here: (i) calbactonite, a calcium material; (ii) febactonites, which are iron derivatives; and (iii) cubactonites, which are copper derivatives. All three forms were produced on *Bacillus subtilis* strains shown previously to be suitable for drawing into threadlike fibers. The electronegative nature of the cell wall in vivo is the basis for metal binding.

The *B. subtilis* cell wall is a gel-like viscoelastic material composed primarily of two polymers: peptidoglycan and teichoic acid (*3*). Both carry ionizable groups that have the potential for metal binding (*4*). Carboxylate groups in the peptide moiety of peptidoglycan are believed to be the primary sites of metal binding (*5*). Cell walls behave as complex ion exchangers. Some bacterial walls have capacities (3.5 milliequivalents per gram) that are equivalent to those of commercial resins such as Dowex A-1 (*6*). Although there is selectivity in the binding of counterions in vivo, cell walls are capable of binding many different ions (*4*, *6*, *7*). Ions such as Fe^{3+}, Cu^{2+}, and Ca^{2+} are known to bind in high quantities (*4*). In living cells, the wall is a multilayered material that is cross-linked into a supramolecular network that encompasses the entire cell (a cylindrical shape about 4 μm long by 0.7 μm in diameter). The *B. subtilis* cell wall is a dynamic structure that is constantly added to on the inner surface and shed on the outside (*8*). The material itself is a flexible porous network of considerable strength (*2*).

The bionites were produced by using derivatives of *B. subtilis* strain FJ7 called 7(II), 7(O), and F3N. The first two strains have been selected for their ability to grow as web cultures from which bacterial threads of uniform diameter can be drawn (*9*). The genetically engineered strain F3N carries the *Escherichia coli* lacZ gene under the control of an unidentified host gene promoter and constitutively produces the enzyme β-galactosidase (*10*). It can also be grown in web form but not as successfully as those selected for that property. Web cultures were grown at 20°C in TB medium (*11*) for ~18 hours. One milliliter of 0.5 M $CaCl_2$, 1 M $FeCl_3$, or 1 M $CuCl_2$ was added to each web culture and dispersed, taking care not to disrupt the integrity of the web. The mixtures were incubated at 23°C for periods indicated in each experiment described below. The mineralized web (Fig. 1, A and B) was then drawn into the room atmosphere at the rate of 5 mm/min with a rate-controlled electric motor (Fig. 1, C to E). The drawing process itself compressed the adherent wet precipitate along with the cellular filaments at the fluid-air interface. The draw rate was chosen to prevent the weight of the wet fiber from exceeding the tensile strength of the bacterial filaments, which is inversely related to their water content. The wet fibers were hung vertically and allowed to dry. Additional fluid drained from them during this process. In

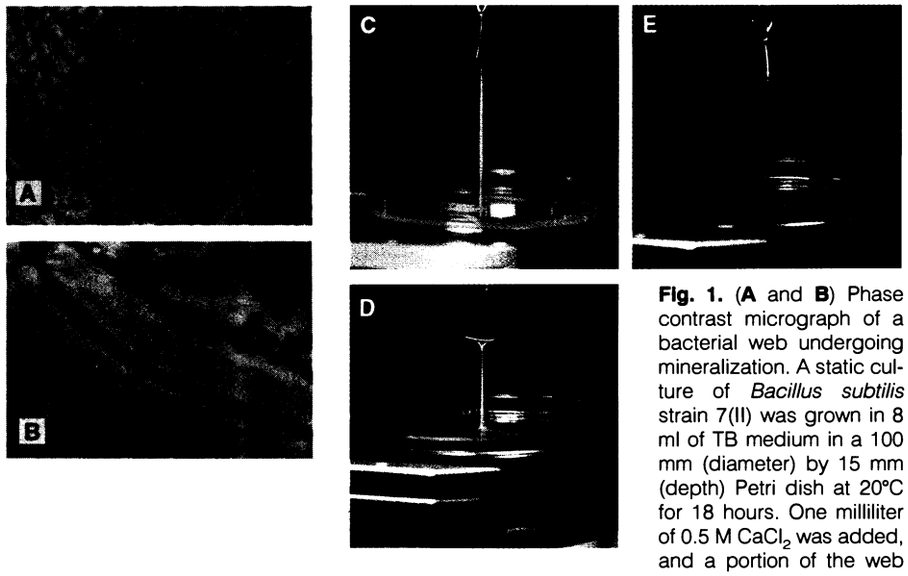

Fig. 1. (**A** and **B**) Phase contrast micrograph of a bacterial web undergoing mineralization. A static culture of *Bacillus subtilis* strain 7(II) was grown in 8 ml of TB medium in a 100 mm (diameter) by 15 mm (depth) Petri dish at 20°C for 18 hours. One milliliter of 0.5 M $CaCl_2$ was added, and a portion of the web was transferred to a microscope slide. (A) A portion of the web with crystals on some cell filaments. (B) A higher magnification view of a single filament with crystals aligned perpendicular to the filament axis. Filament diameter in both is 0.7 μm. (**C** to **E**) Bionites being drawn from mineralized webs of *B. subtilis*. Fibers were drawn after 1 hour of mineralization of web cultures with (C) $CaCl_2$, (D) $FeCl_3$, and (E) $CuCl_2$. Draw rate was 5 mm/min. Petri dish diameter is 100 mm.

Department of Molecular and Cellular Biology, University of Arizona, Tucson, AZ 85721.